Supporting Information

Precatalytic Surface Roughness of Fe-Modified Ni Electrodes Translates into Intrinsic Sites for Oxygen Evolution Reactivity

Ramadan Chalil Oglou[†], Morten Linding Frederiksen[‡§], Paul Maurice Leidinger[†], Marcel Ceccato[†], Anders Bentien[‡], Jeppe V. Lauritsen[†*]

[†]*Interdisciplinary Nanoscience Center, Aarhus University, 8000 Aarhus C, Denmark*

[‡]*Department of Biological & Chemical Engineering, Aarhus University, 8200 Aarhus N, Denmark*

[§]*HydrogenPro ApS, 8270 Højbjerg, Denmark*

*Corresponding author email: jvang@inano.au.dk

Contents

Supplementary Note 1: Electrochemical Tests of NF Electrodes

Electrochemical tests of the NF electrodes were conducted using a Biologic SP-50e electrochemical workstation. Three-electrode measurements were carried out in Fe-purified 1 M potassium hydroxide (KOH)[1], where the Ni foam (1 × 1 cm^2) served as both the working electrode (WE) and counter electrode (CE), and a Hg/HgO electrode was used as the reference electrode (RE). Cyclic voltammetry (CV) was performed in the potential range of 0.15 to 0.70 V vs. Hg/HgO at a scan rate of 5 mV s^{-1}, with all potentials subsequently converted to the reversible hydrogen electrode (RHE) scale. The following equation is used for conversion:

$$E_{RHE} = E_{Hg/HgO}\,(V) + 0.059 \times pH + E^{o}_{Hg/HgO}\,(V) \qquad (1)$$

pH is 14 for the 1 M KOH electrolyte, and $E°_{Hg/HgO}$ is 0.14 V at 25 °C.

All electrochemical data were iR-corrected and the current was normalized to geometric area. The uncompensated resistance (R_u) was determined using electrochemical impedance spectroscopy (EIS) by identifying the minimum impedance point at high frequencies.

Tafel slopes were extracted from multistep chronopotentiometry (MUSCP) measurements, in which the current was held from 0.01 to 10 mA for 15 minutes, and the average potential over the last 20 seconds at each step was used as a datapoint[2,3].

The electrochemical surface area (ECSA) was estimated by calculating the double-layer capacitance (C_{dl}) in an aprotic electrolyte consisting of 0.15 M potassium

hexafluorophosphate (KPF_6) in acetonitrile (MeCN). This choice of electrolyte avoids additional current contributions arising from ion transfer reactions at the electrode interface, such as corrosion, intercalation, or specific adsorption, which are common in aqueous media[3]. An H-cell separated by a porous frit was used, with a platinum mesh as the counter electrode and a silver wire enclosed with MeCN was used as the reference. The electrolyte was purged with N_2 prior to measuring, and a constant flow was held in the headspace during the measurement. Anodic (j_a) and cathodic (j_c) current densities were recorded at various scan rates (ν) and used to estimate C_{dl} by fitting the data to either an ideal capacitor model:

$$j = C_{dl} \times \nu \qquad (2)$$

or an allometric model assuming a constant phase element:

$$j = C_{dl} \times \nu^{\alpha} \qquad (3)$$[4].

Two-electrode cell measurements were carried out using 2 × 2 cm^2 identical NF electrodes as both the anode and cathode, separated by a commercial OH^--permeable membrane analogous to AGFA's ZIRFON. The electrodes were immersed in 30 wt% KOH electrolyte maintained at 90 °C, following the procedures used in our previous study[2]. The stability of the pristine and acid-treated NF electrodes was evaluated by applying a constant current density of 200 mA cm^{-2} over a period of 140 hours.

Supplementary Note 2: Electrochemical Tests of Modified-Ni(111) Crystals

Electrocatalytic activity measurements of single crystal model systems were conducted in a UHV-compatible electrochemical cell, which enables the transfer of a single-crystal sample plate from the UHV environment to the electrochemical setup without exposure to ambient conditions[5]. To eliminate air exposure and prevent contamination, the electrolyte (0.1 M NaOH, 99.99% purity) was saturated with inert gas for at least 30 minutes, and the electrochemical cell was also purged with argon gas. This procedure ensures reliable post-UHV characterizations free from atmospheric contaminants. A three-electrode configuration was employed for the electrochemical studies, with the Ni(111) single crystal serving as the working electrode (WE). A Ni wire (≥99.99%) was used as the counter electrode (CE), while a leak-free Ag/AgCl electrode (LF-1.6-100, Innovative Instruments Ltd.) functioned as the reference electrode (RE). Following electrochemical testing, the sample was thoroughly rinsed with deionized water inside the cell to minimize NaOH contamination. Linear sweep voltammetry (LSV) measurements were performed in the potential range of 0.2 to 0.8 V vs. Ag/AgCl at a scan rate of 20 mV s^{-1}, and the recorded current was normalized to the geometric area of the crystal. The potential measured against the Ag/AgCl reference electrode ($E_{Ag/AgCl}$) is converted into potential against the E_{RHE} using the following equation:

$$E_{RHE} = E_{Ag/AgCl}(V) + 0.059 \times pH + E^{o}_{Ag/AgCl}(V) \qquad (4)$$

pH is 13 for the 0.1 M NaOH electrolyte, and $E°_{Ag/AgCl}$ is 0.1976 V at 25 °C.

Tafel analysis was carried out using the linear region of the LSV curves, where the initial rise in current corresponds to the onset of the OER. Only the potential range exhibiting linear current–overpotential behavior on a semi-logarithmic scale was considered, while the higher current region—where deviation from linearity occurs due to mass transport limitations or bubble formation—was excluded from the fitting.

Supplementary Note 3: Condensed H_2O Droplet Preparation for Ni(111) Crystals

The condensed H_2O droplet was prepared in a small chamber, mounted to the main UHV system, with a base pressure of 1×10^{-7} mbar. Following a previously established methodology[6,7], the chamber was equipped with a highly localized cold spot designed for ice growth, commonly referred to as a "cold finger". The temperature on this spot was maintained near liquid nitrogen (LN_2) temperature to minimize H_2O vapor pressure. The tip of the cold finger was cooled using an LN_2 flow for 10 minutes, after which H_2O vapor was introduced for 1 minute via a valve connected to a mounted $H_2O(l)$ reservoir at room temperature. Due to localized cooling, an icicle formed immediately at the tip of the cold finger. Subsequently, the sample was positioned beneath the cold finger, and LN_2 cooling was discontinued. The system was then gradually warmed using a heat gun, allowing the icicle to melt over a few minutes and deposit as a liquid droplet onto the crystal surface. Following this process, the chamber was evacuated, and once an adequate pressure level was reached, the sample was transferred back to the main UHV chamber for further characterization.

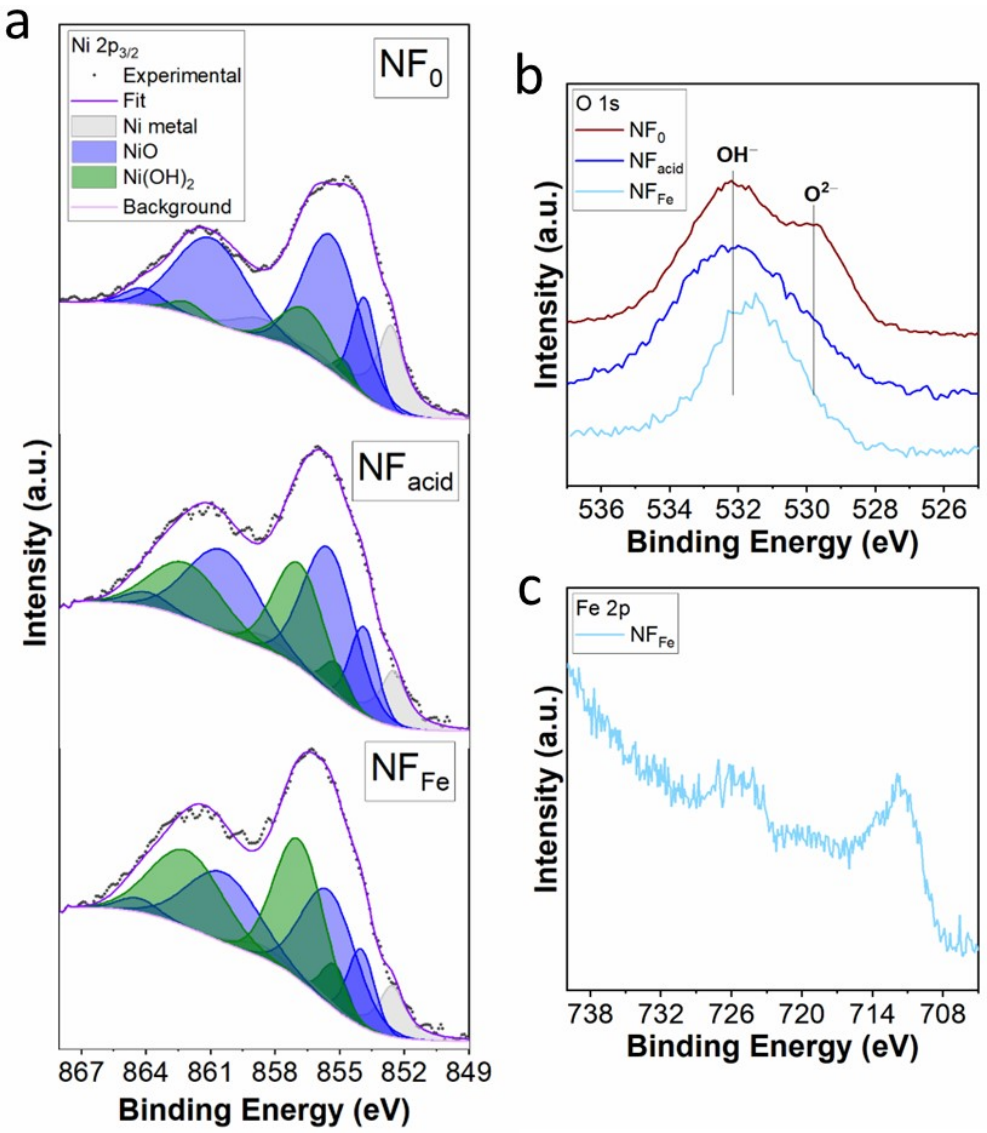

Supplementary Fig. 1: a, Fitted Ni $2p_{3/2}$ and **b**, O 1s XPS spectra of NF_o, NF_{acid}, and NF_{Fe} electrodes prior to any electrochemical conditioning. **c**, Fe 2p spectrum of the NF_{Fe} electrode prior to any electrochemical conditioning. XPS analysis of the Ni $2p_{3/2}$ signal showed a significant reduction in NiO content after acid treatment, with the surface chemistry shifting predominantly toward $Ni(OH)_2$ formation in the samples NF_{acid} and NF_{Fe} (a). This transformation was further supported by the O 1s spectra, which indicated a substantial decrease in lattice oxygen following acid treatment (b). Moreover, the relative metal composition (Ni and Fe) was determined using the area of the metal $2p_{3/2}$ peaks, including the main satellites, a Shirley background, and relative sensitivity factors provided by CasaXPS software. Fe spraying on NF led to the formation of FeOOH species, resulting in a Ni:Fe ratio of 1.7 (c).

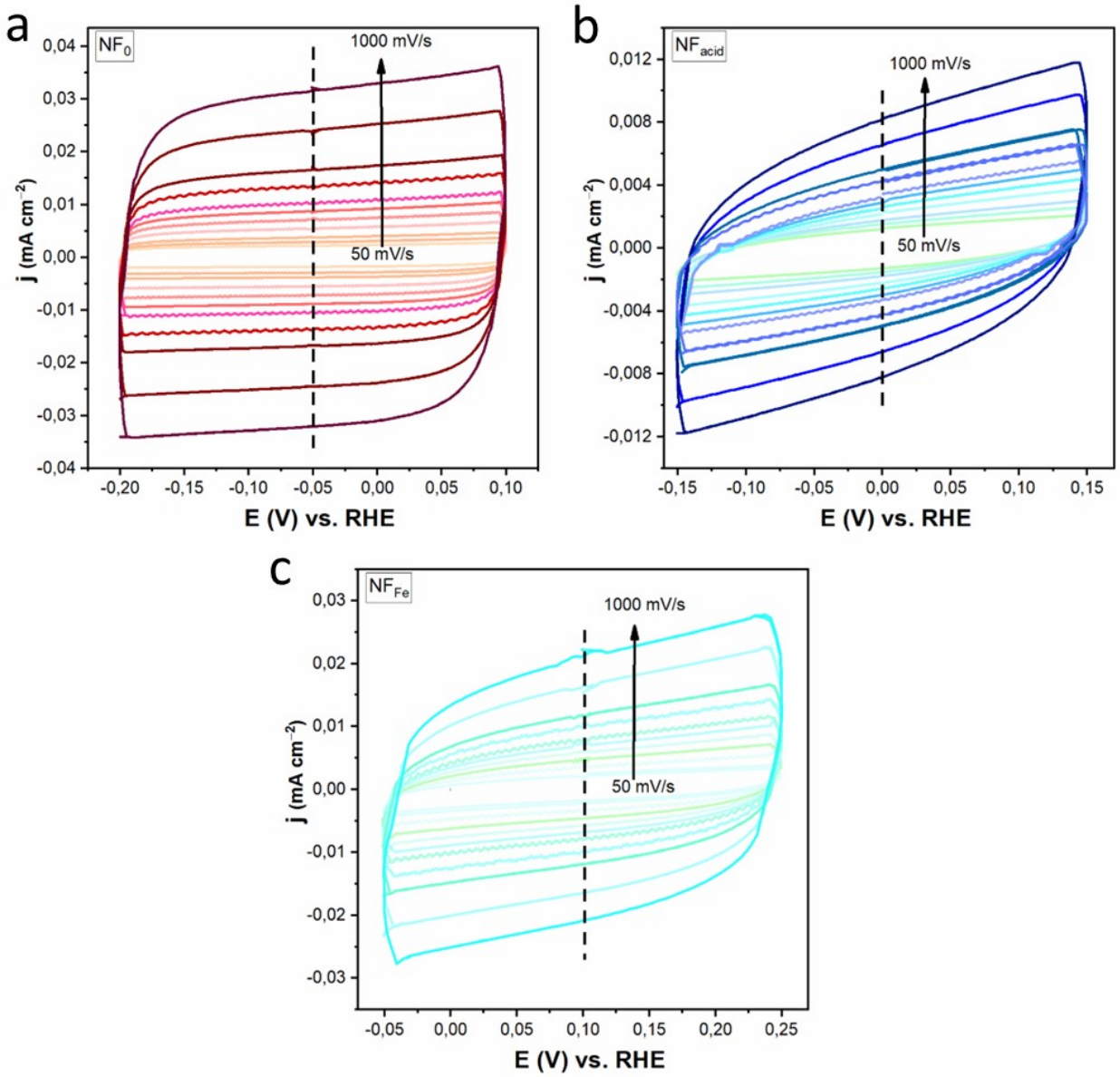

Supplementary Fig. 2: CV recordings in 0.15 M KPF_6 in MeCN within the non-Faradaic region at varying scan rates (50 to 1000 mV s^{-1}) for **a**, NF_o, **b**, NF_{acid}, and **c**, NF_{Fe} electrodes. The vertical dashed lines indicate the potentials at which both anodic and cathodic currents were measured for ECSA estimation.

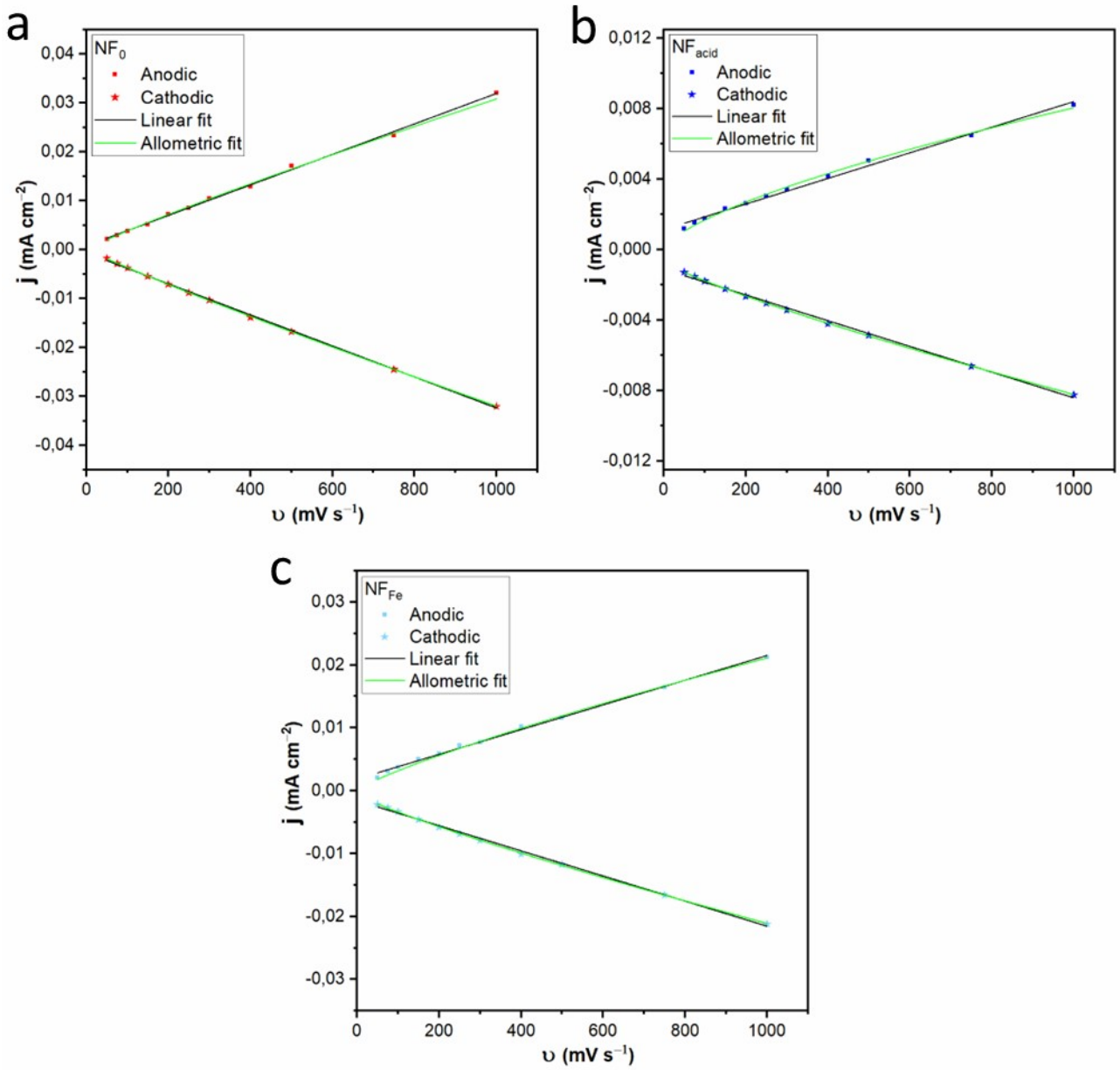

Supplementary Fig. 3: The j vs. ν relationships with corresponding fittings for **a**, NF_o, **b**, NF_{acid}, and **c**, NF_{Fe} electrodes. Linear fittings are shown in black, while allometric fittings are shown in green.

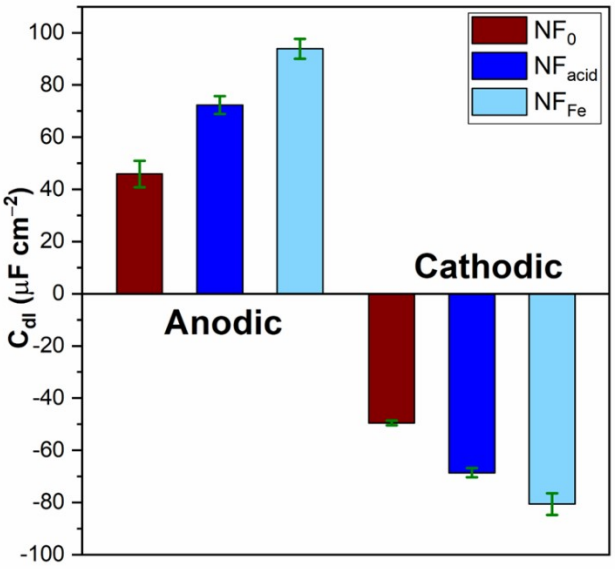

Supplementary Fig. 4: Double layer capacitance (C_{dl}) values for NF electrodes estimated from allometric model.

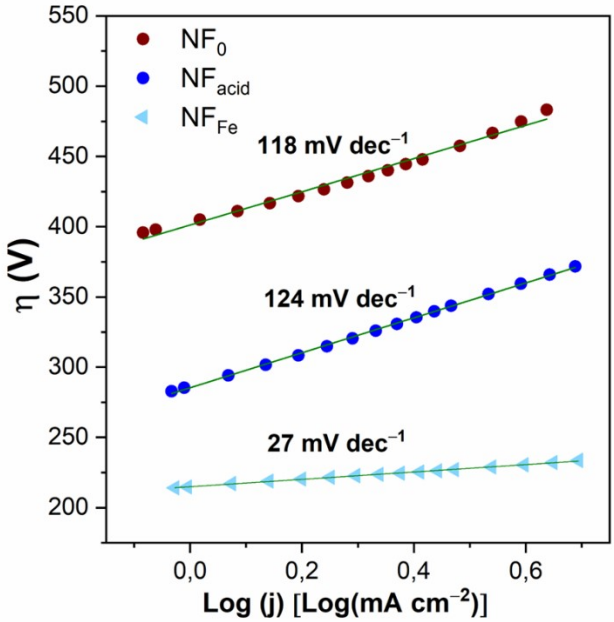

Supplementary Fig. 5: Tafel analysis of NFs electrodes extracted from multistep chronopotentiometry measurements in 1 M Fe-purified KOH.

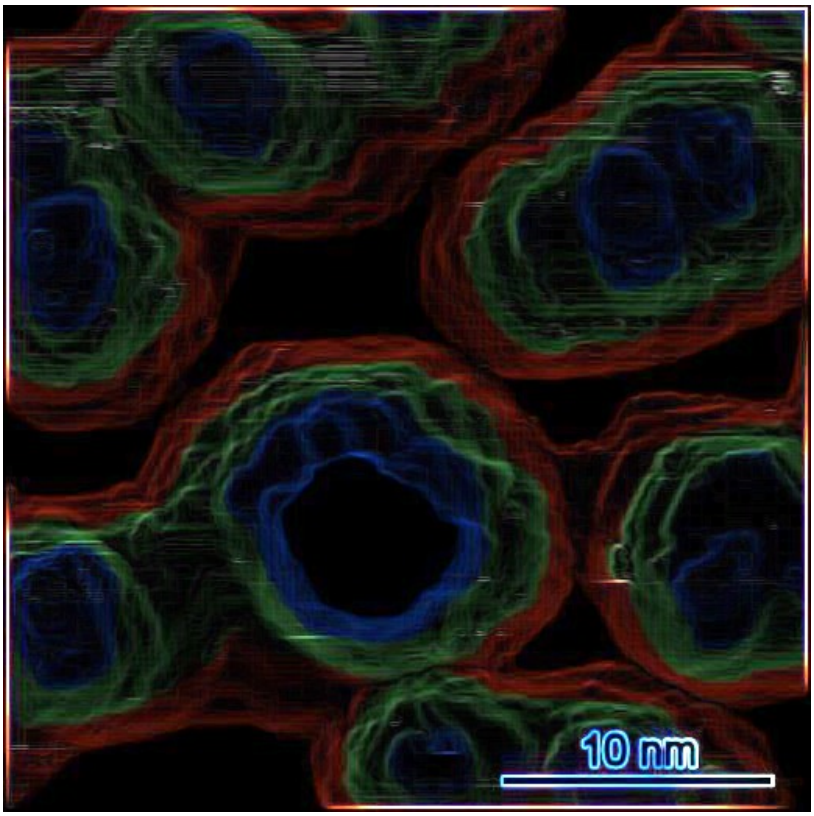

Supplementary Fig. 6: The STM image of the $Ni(111)_{step}$ sample. V_t = 0.07 V, I_t = 0.97 nA. A vertical intensity color gradient was applied to enhance the visibility of variations in step-edge density within the clusters formed after Ar^+ sputtering.

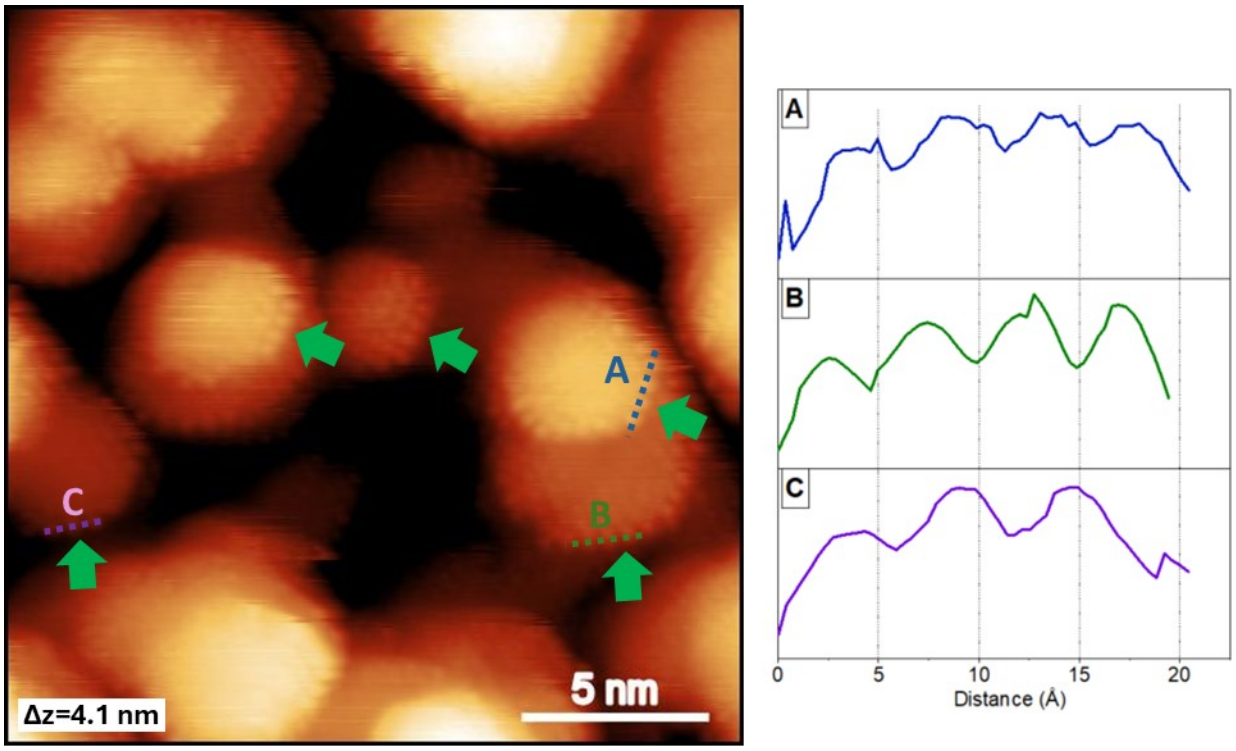

Supplementary Fig. 7: The STM image of Fe/Ni(111)$_{step}$ sample. V_t = -0.05 V, I_t = -1.17 nA. The green arrows indicate the anchored Fe atoms at the perimeter (edge sites) of the hillocks of Ni(111)$_{step}$. The Δz value given in the image indicates the total topographical height range of the image. The line scans indicate the distances between the anchored Fe atoms on Ni clusters. Fe atoms are located at the perimeter of the Ni clusters, where the edge structure exhibits a double atomic spacing relative to Ni atoms. Given the larger atomic radius of Fe compared to Ni, Fe atoms preferentially bind to Ni step edges, likely assuming alternating double-periodicity along the Ni sites, corresponding to distances of 5 Å.

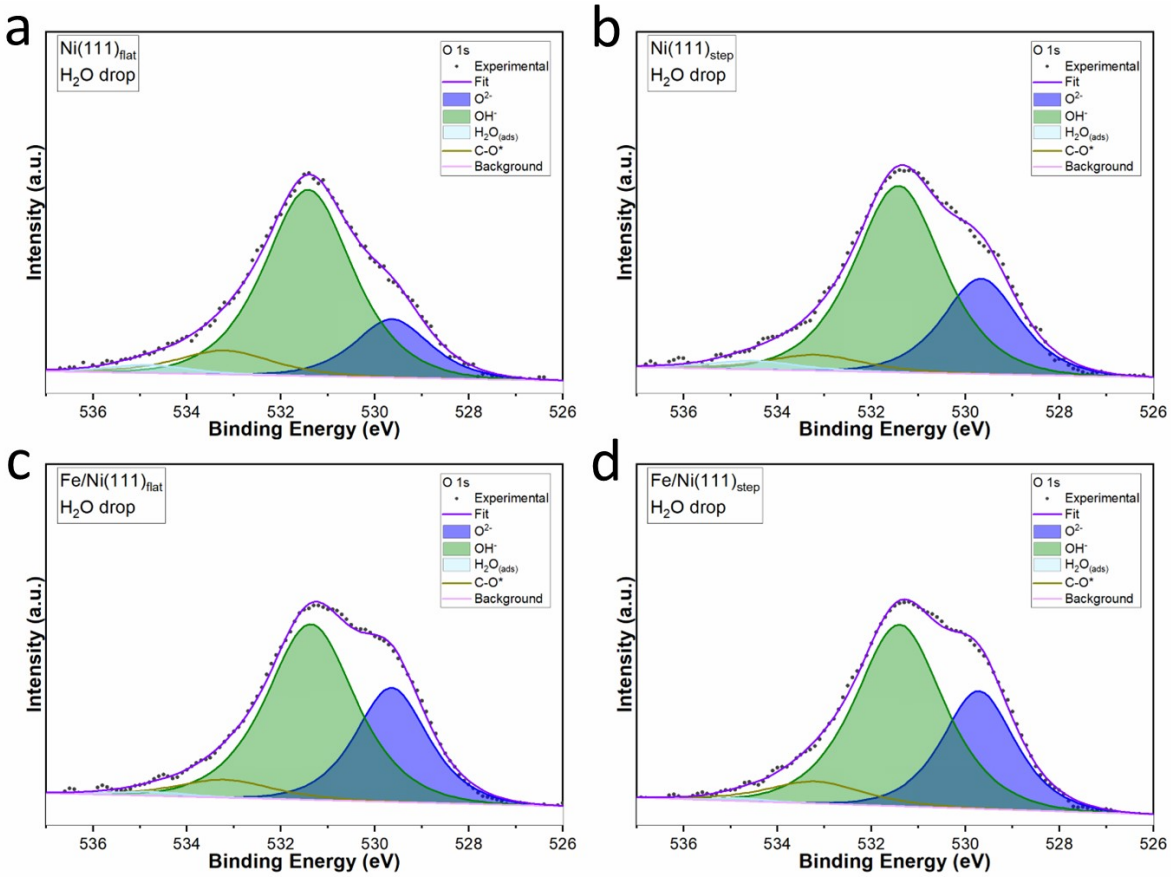

Supplementary Fig. 8: The fitted O 1s signals for post-H_2O dropped **a**, $Ni(111)_{flat}$, **b**, $Ni(111)_{step}$, **c**, $Fe/Ni(111)_{flat}$, and (d) $Fe/Ni(111)_{step}$.

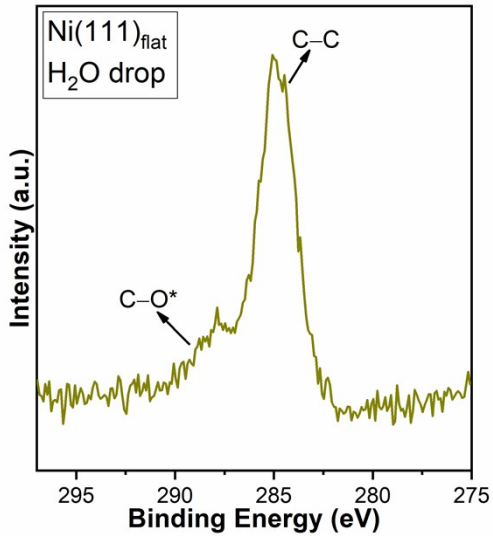

Supplementary Fig. 9: The C 1s signal for $Ni(111)_{flat}$ after H_2O droplet exposure, attributed to minor carbon contaminants originating from the liquid.

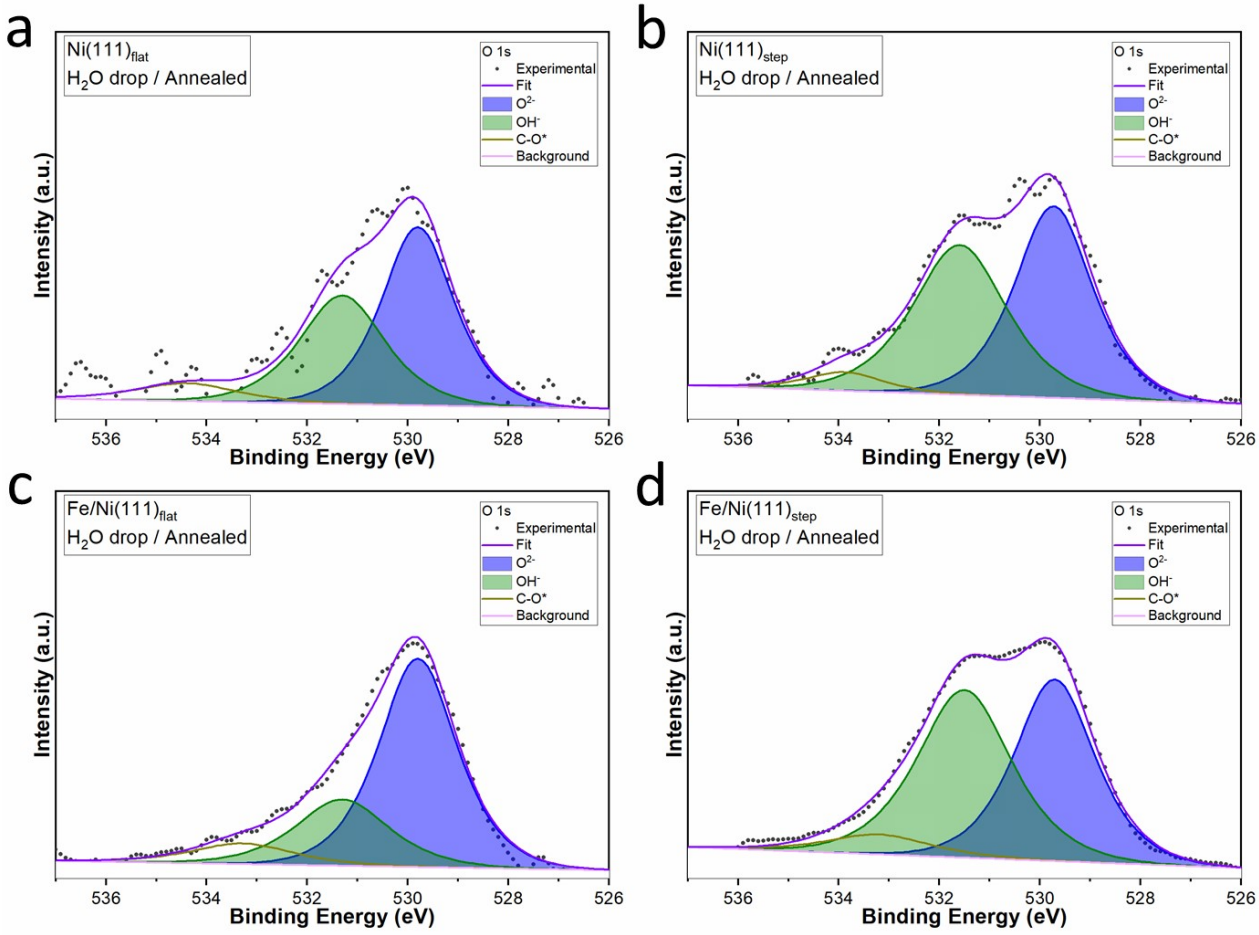

Supplementary Fig. 10: The fitted O 1s signals for post-annealed and H_2O droplet exposed **a**, $Ni(111)_{flat}$, **b**, $Ni(111)_{step}$, **c**, $Fe/Ni(111)_{flat}$, and **d**, $Fe/Ni(111)_{step}$.

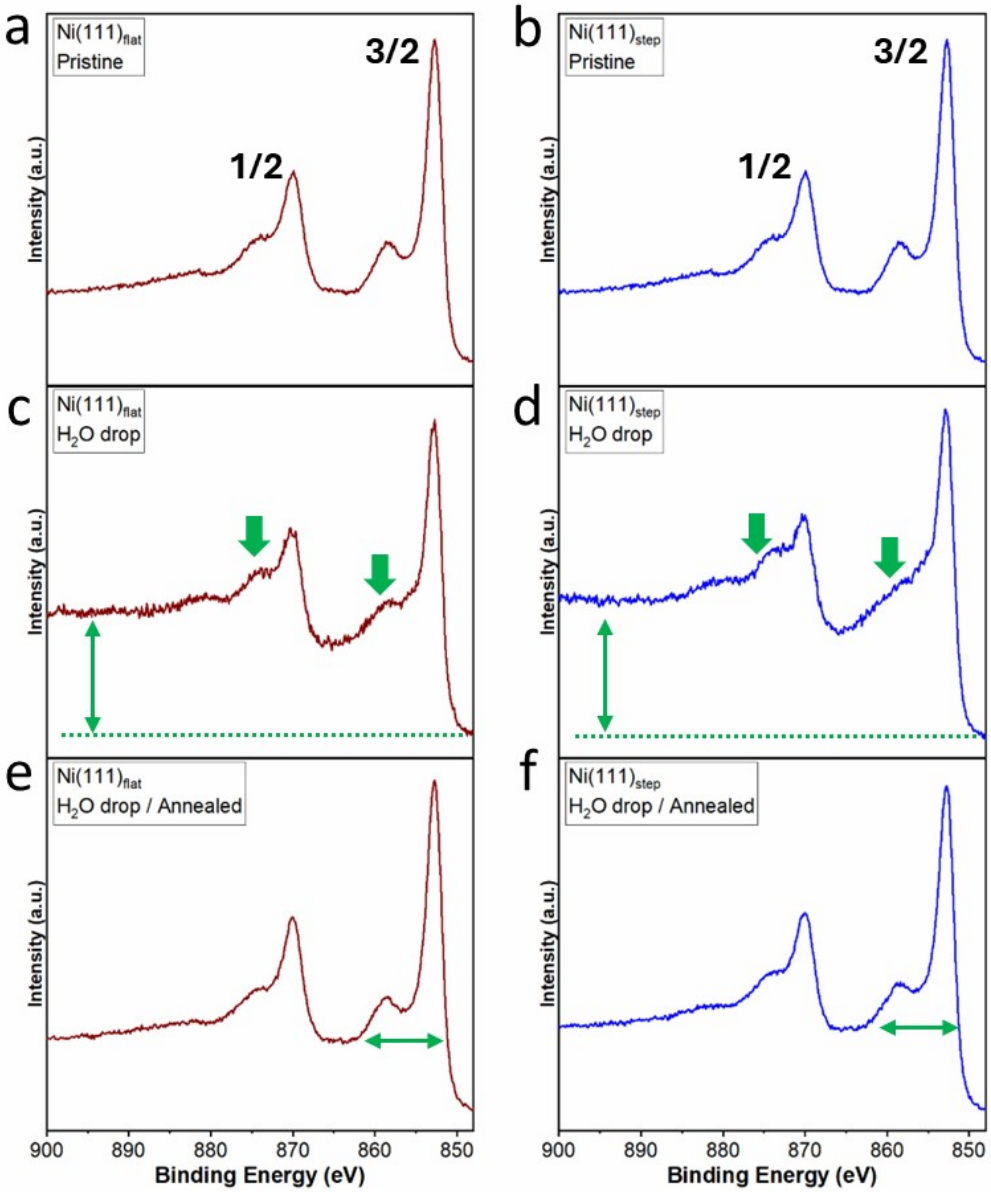

Supplementary Fig. 11: The Ni 2p signals for (**a,b**) pristine, (**c,d**) post-H_2O drop and (**e,f**) post-annealed H_2O drop of $Ni(111)_{flat}$ and $Ni(111)_{step}$. Given that XPS surface sensitivity extended beyond 5 monolayers (ML) for the used photon energy, the Ni 2p signal predominantly reflects the metallic state. The pristine Ni 2p spectra exhibit well-defined spin-orbit splitting for the metallic Ni state (a,b). Following H_2O droplet exposure, a slight increase in the background intensity is observed due to the formation of surface species, along with a suppression of the Ni satellite peaks at ~875 eV ($2p_{1/2}$) and ~858 eV ($2p_{3/2}$) (indicated by arrows). This is indicative of a partial Ni oxidation (c,d). Upon annealing at 500 K, the spectra closely resemble those of pristine metallic Ni, confirming the desorption of surface species (e,f). However, the $Ni(111)_{step}$ sample exhibits a 1.2 eV peak broadening

toward higher binding energy, consistent with the presence of a higher level of oxidized Ni species compared to $Ni(111)_{flat}$.

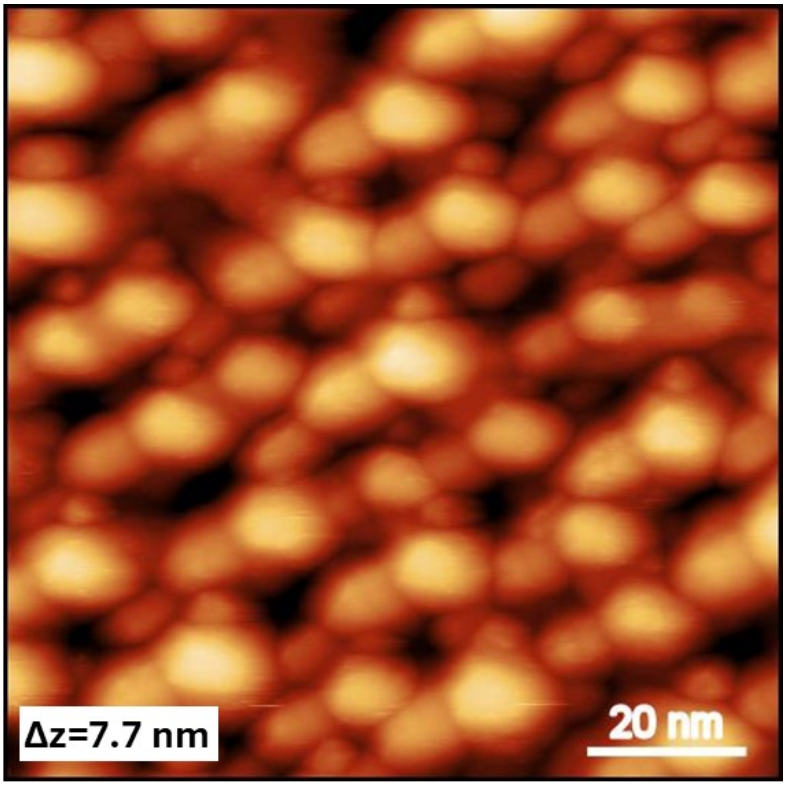

Supplementary Fig. 12: Large-scale STM image of H_2O droplet exposed and post-annealed $Ni(111)_{step}$. V_t = -0.10 V, I_t = -1.35 nA.

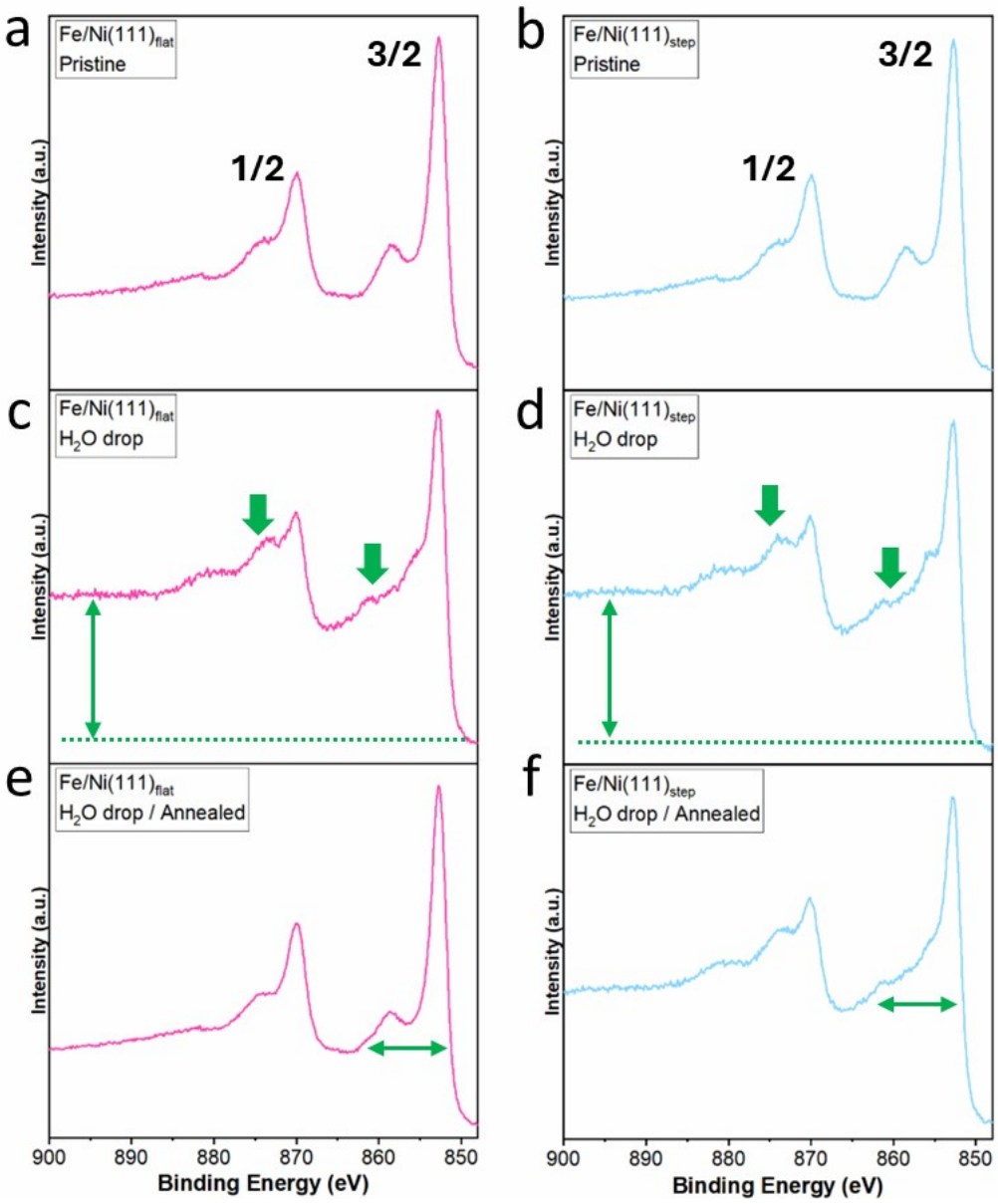

Supplementary Fig. 13: The Ni 2p signals for (**a,b**) pristine, (**c,d**) post-H_2O drop and (**e,f**) post-annealed H_2O drop of $Fe/Ni(111)_{flat}$ and $Fe/Ni(111)_{step}$. The pristine Ni 2p spectra show clear spin-orbit splitting characteristic of metallic Ni (a, b). After H_2O droplet exposure, we observe a slight increase in background intensity along with suppression of the Ni satellite peaks at ~875 eV ($2p_{1/2}$) and ~858 eV ($2p_{3/2}$) (indicated by arrows), indicating partial surface oxidation (c, d). Annealing the sample at 500 K largely restores the metallic Ni spectral width (indicated by horizontal arrows), confirming the desorption of surface species (e, f). In contrast, the $Fe/Ni(111)_{step}$ sample displays a 4.5 eV broadening of the Ni 2p peak toward higher binding energies, suggesting the presence of more strongly oxidized Ni species relative to the $Fe/Ni(111)_{flat}$ surface.

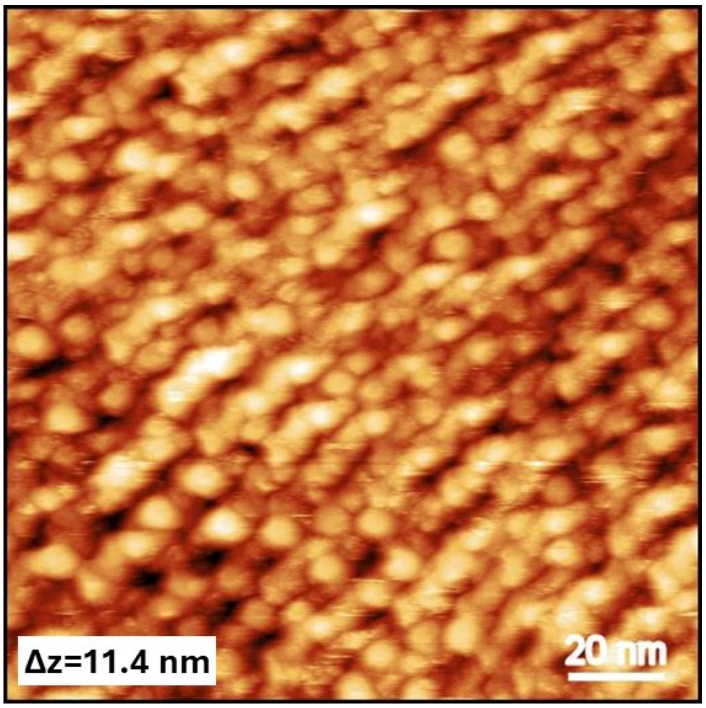

Supplementary Fig. 14: The STM image of post-annealed H2O drop Fe/Ni(111)$_{step}$. V_t = -1.25V, I_t = -0.89 nA.

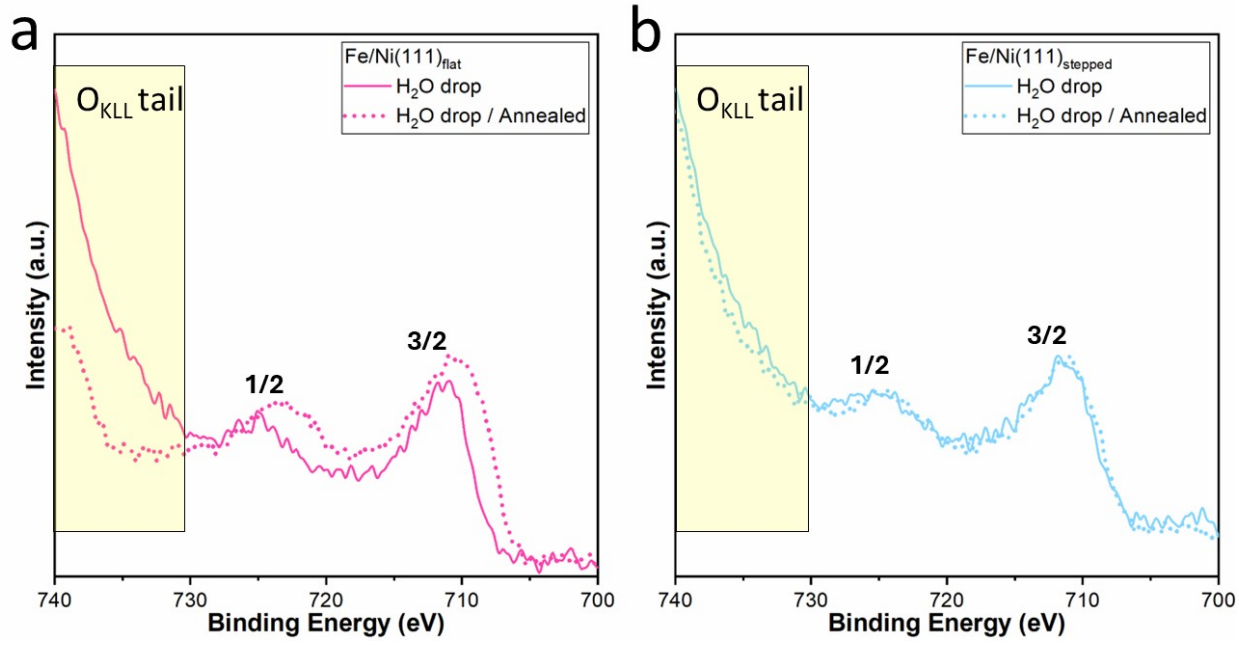

Supplementary Fig. 15: The Fe 2p signals for post-H_2O drop and post-annealed H_2O drop of **a**, Fe/Ni(111)$_{flat}$ and **b**, Fe/Ni(111)$_{step}$. The overlapping shoulder of O_{KLL} Auger peak with Fe 2p region appears in the 730–740 eV binding energies.

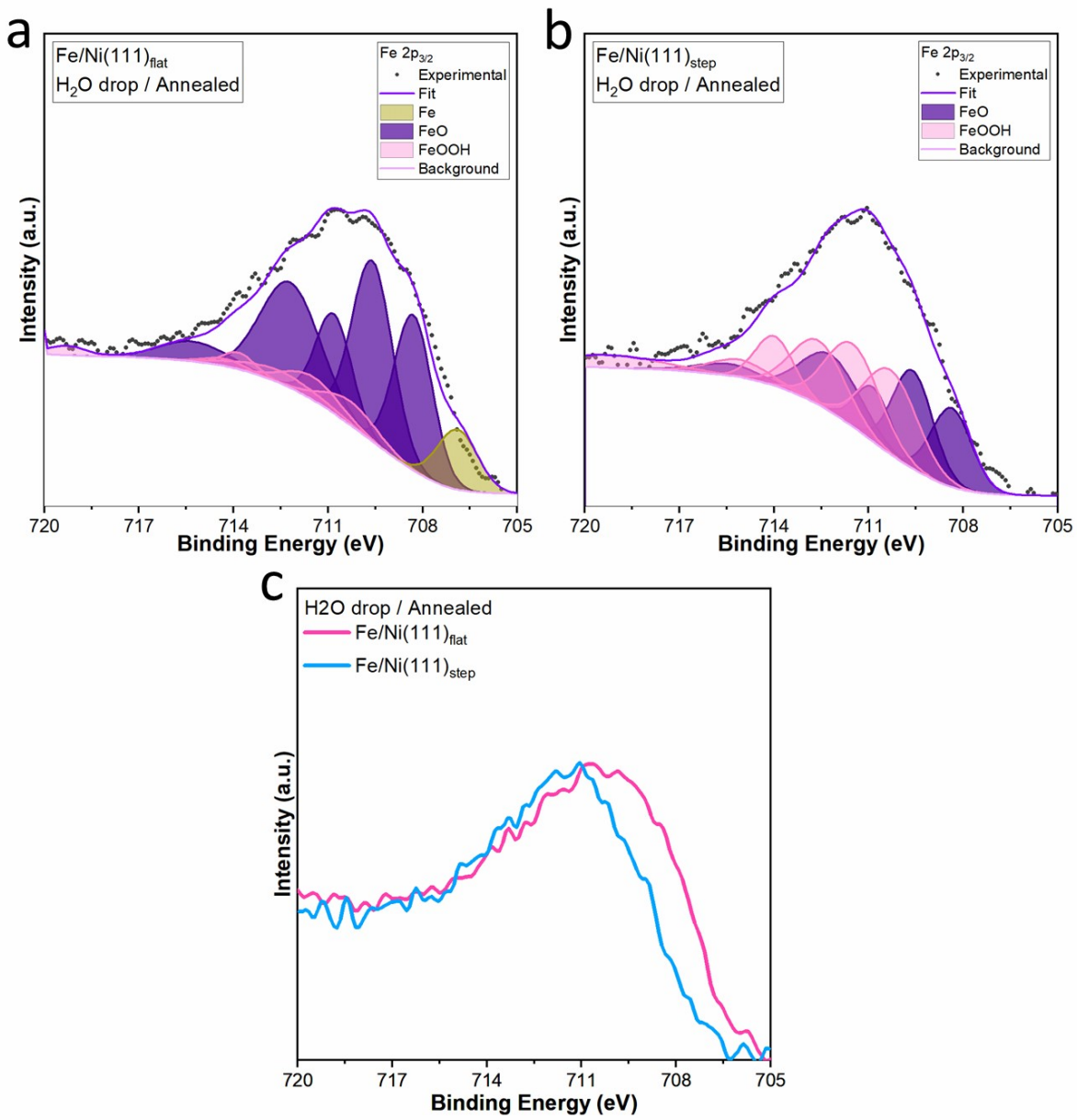

Supplementary Fig. 16: The fitted post-annealed H_2O drop Fe 2p signals for **a**, Fe/Ni(111)$_{flat}$ and **b**, Fe/Ni(111)$_{step}$. **c,** the Fe $2p_{3/2}$ raw data of the two samples are shown to confirm the peak position and full-width-half-maximum (FWHM) changes. For the fittings, the peak positions and relative intensities were constrained according to the references[8,9]. Minor metallic Fe^0 in Fe/Ni(111)$_{flat}$ present in the fit likely reflected subsurface Fe atoms near the interface between the Ni metal and the skin oxide layer.

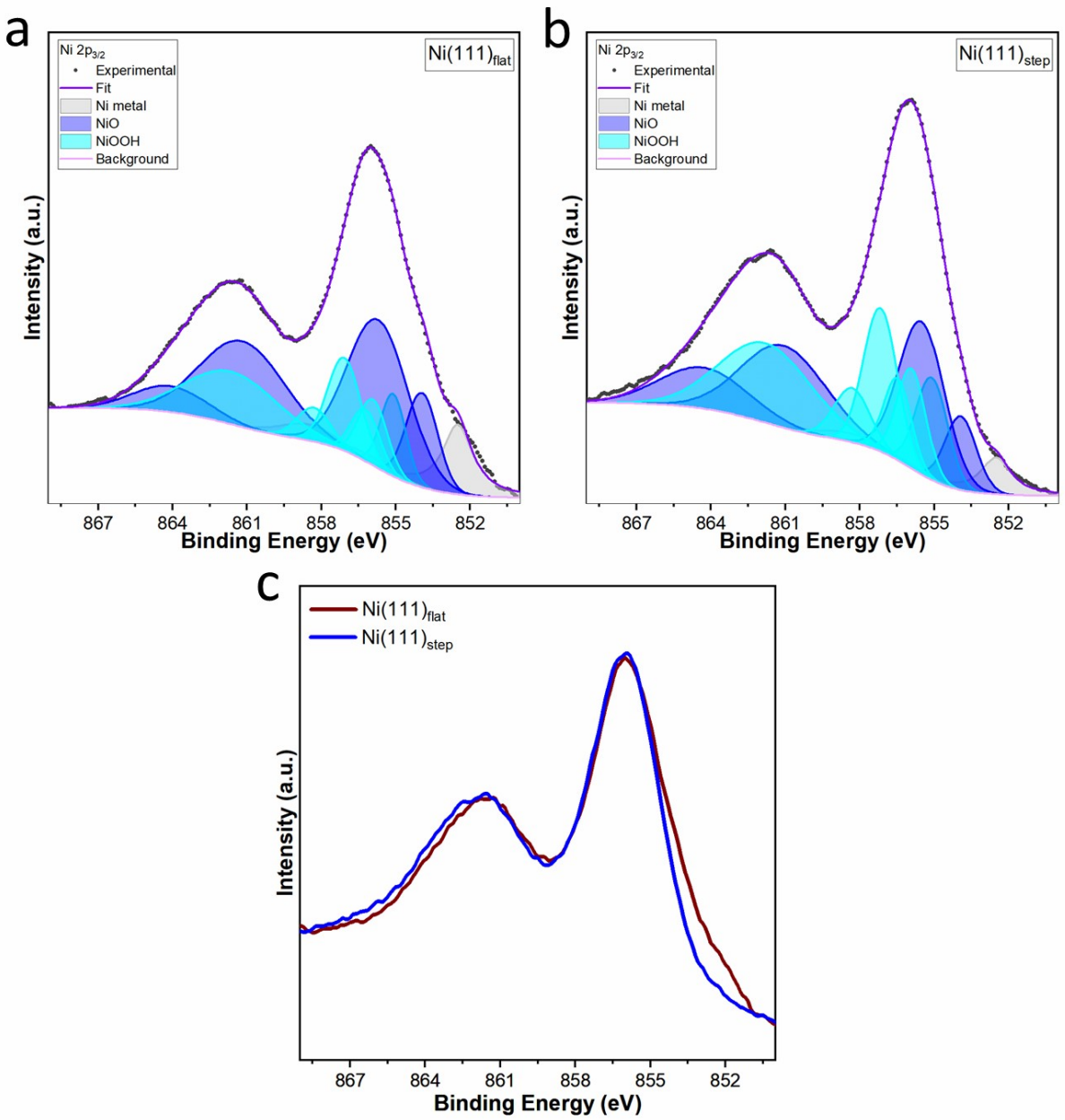

Supplementary Fig. 17: The fitted Ni $2p_{3/2}$ signals for **a**, $Ni(111)_{flat}$ and **b**, $Ni(111)_{step}$ after OER. **c**, the Ni $2p_{3/2}$ raw data of the two samples are shown to confirm the FWHM changes.

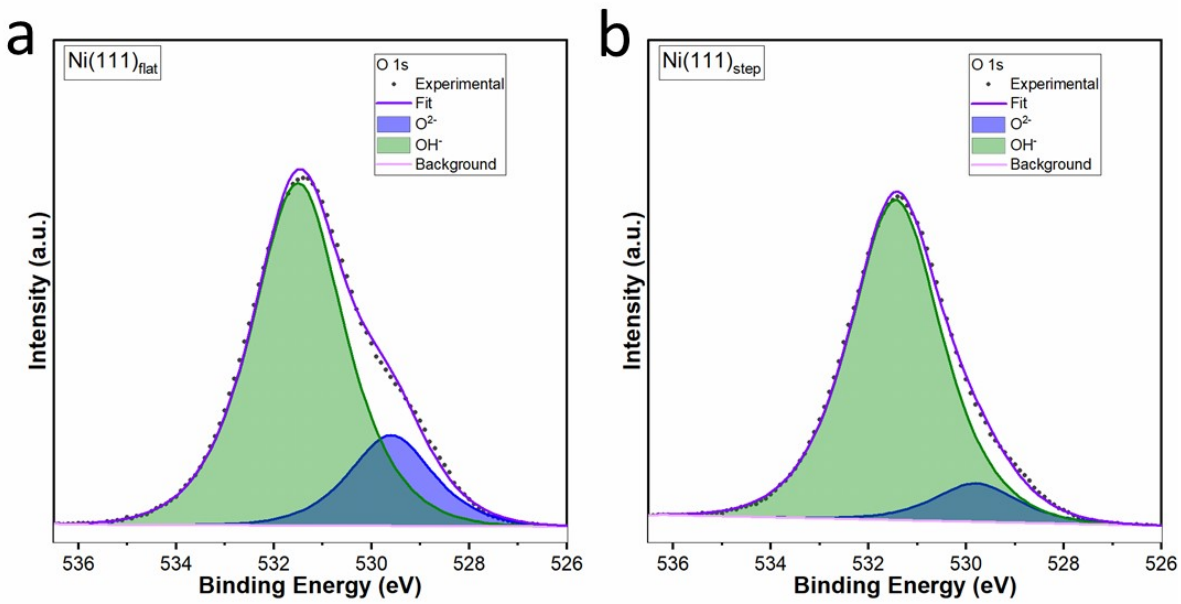

Supplementary Fig. 18: The fitted O 1s signals for **a**, $Ni(111)_{flat}$, and **b**, $Ni(111)_{step}$ after OER.

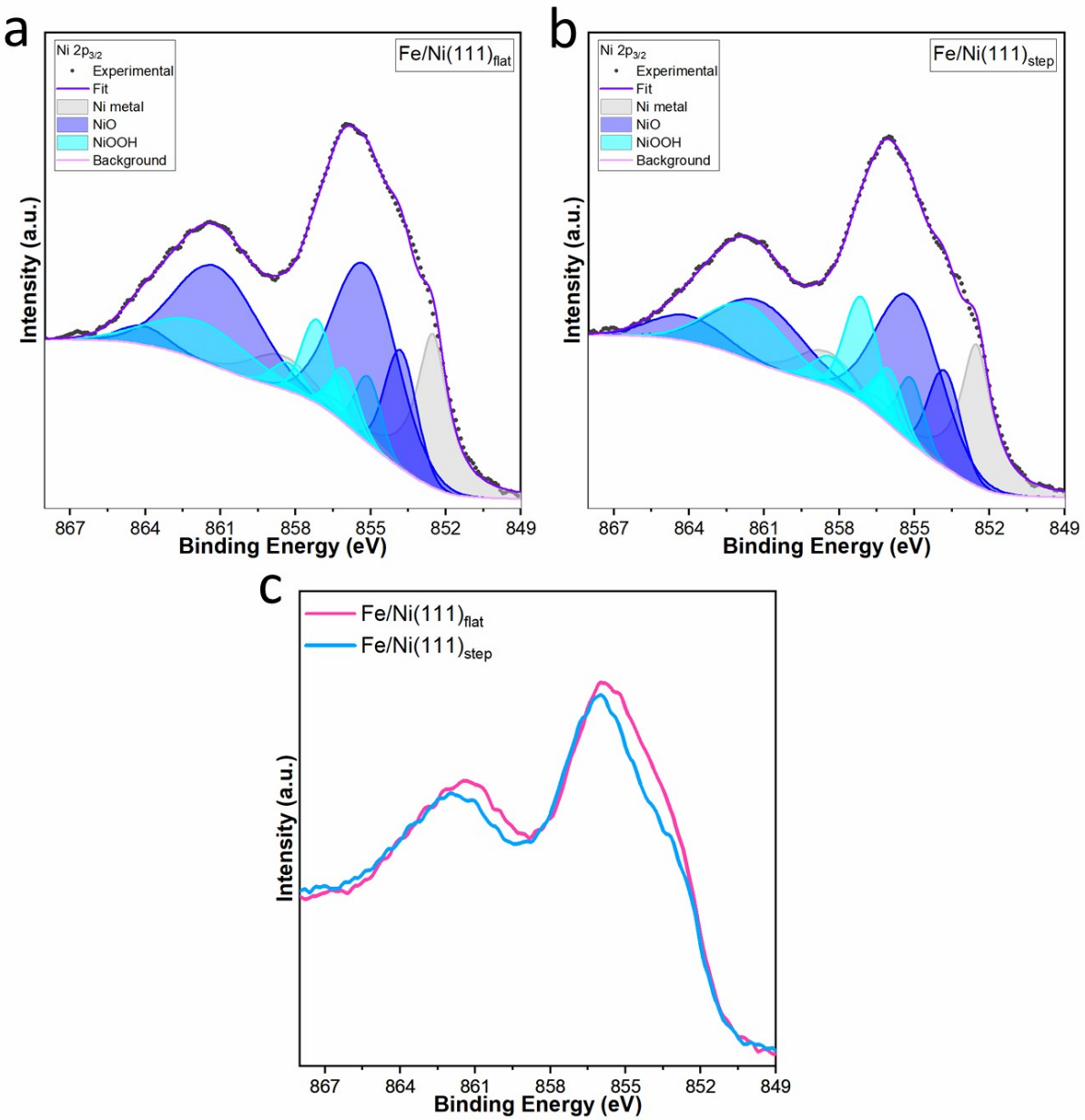

Supplementary Fig. 19: The fitted Ni $2p_{3/2}$ signals for **a**, Fe/Ni(111)$_{flat}$ and **b**, Fe/Ni(111)$_{step}$ after OER. **c,** the Ni $2p_{3/2}$ raw data of the two samples are shown to confirm the FWHM changes.

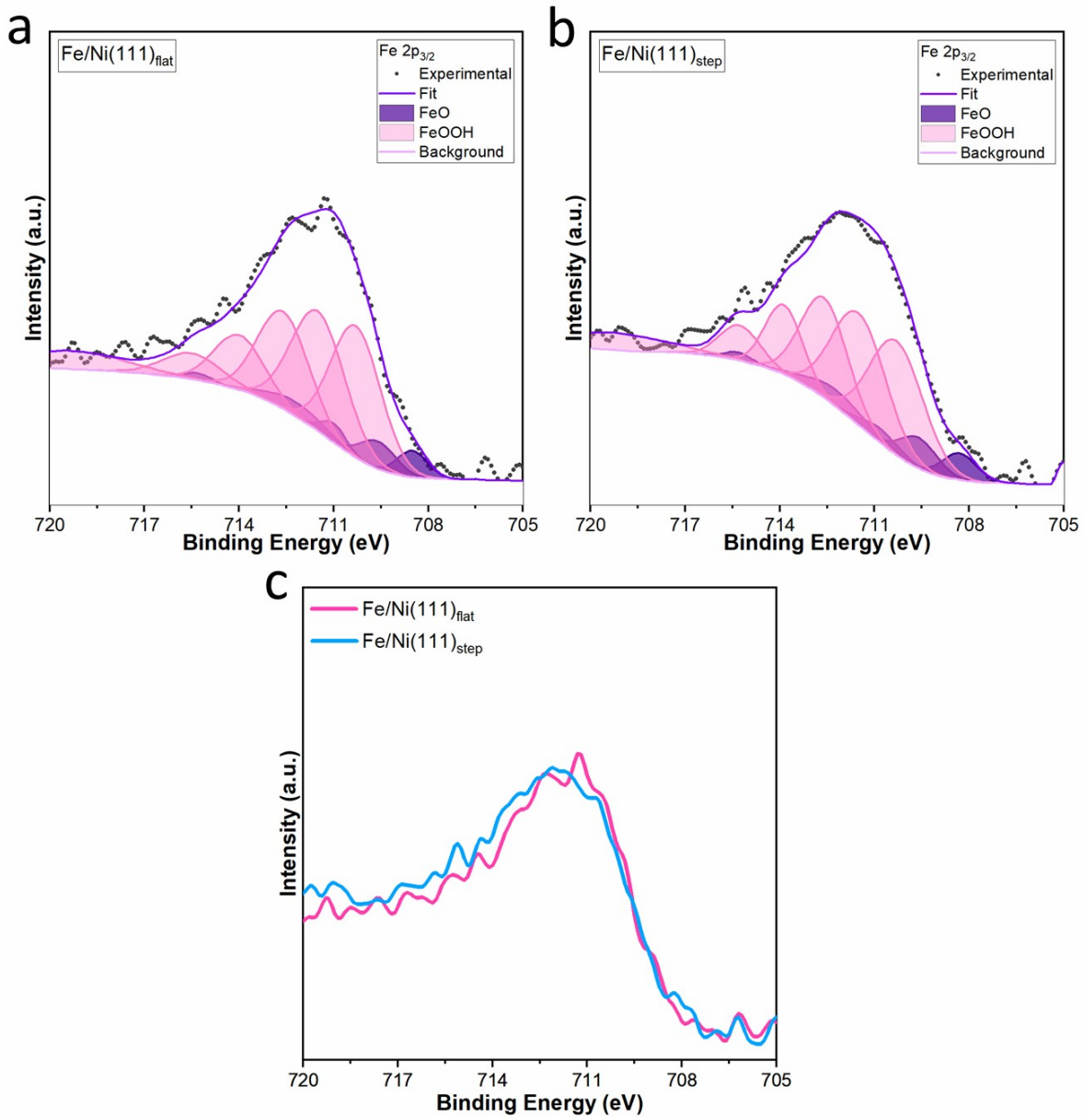

Supplementary Fig. 20: The fitted Fe $2p_{3/2}$ signals for **a**, Fe/Ni(111)$_{flat}$ and **b**, Fe/Ni(111)$_{step}$ after OER. **c,** the Fe $2p_{3/2}$ raw data of the two samples are shown to confirm that the FWHMs don't change.

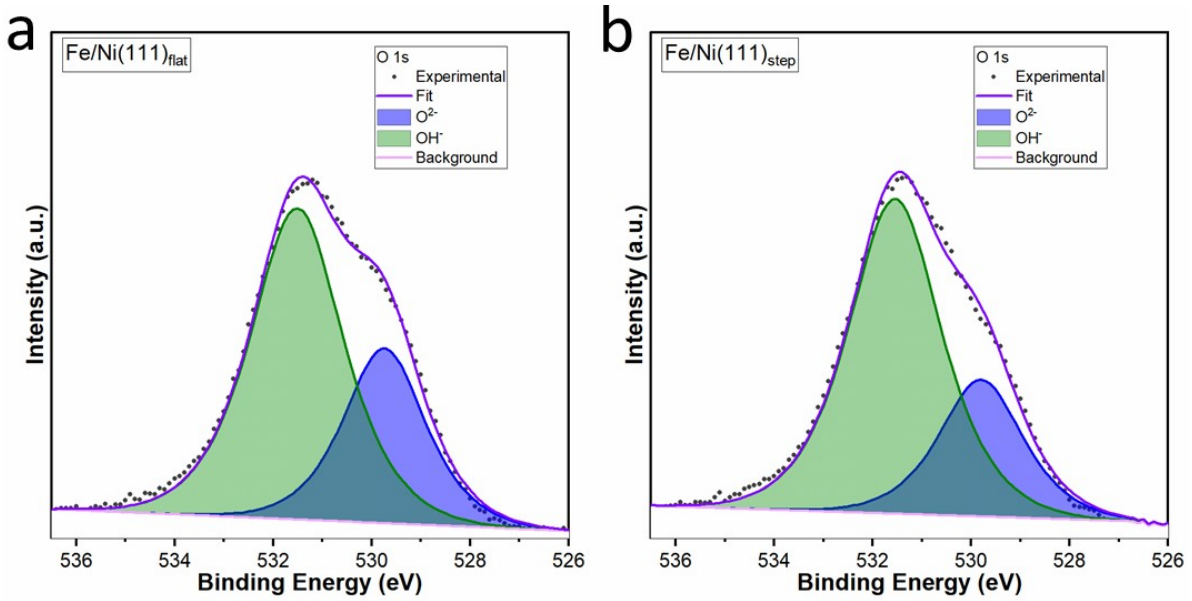

Supplementary Fig. 21: The fitted O 1s signals for **a**, Fe/Ni(111)$_{flat}$, and **b**, Fe/Ni(111)$_{step}$ after OER.

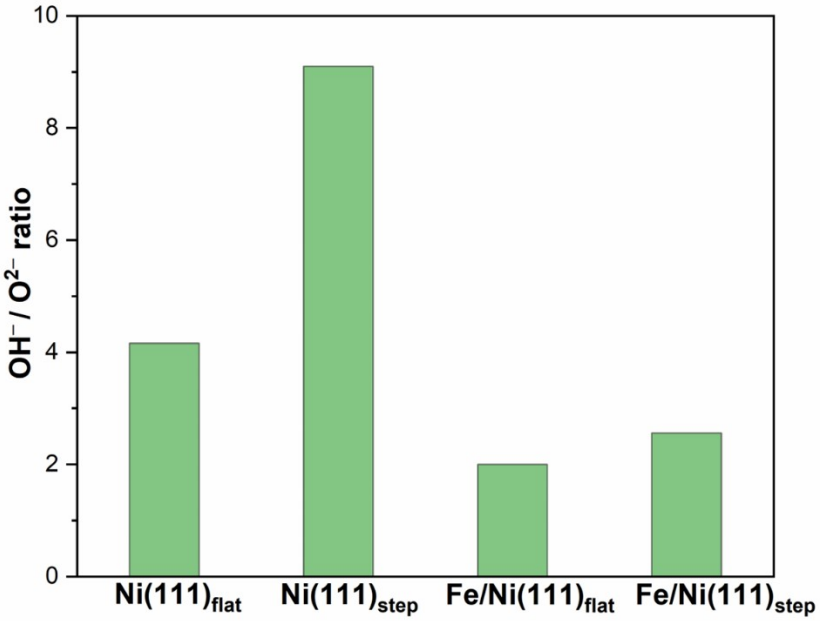

Supplementary Fig. 22: The post-OER OH^-/O^{2-} ratios obtained from O 1s signals based on the fittings of samples.

Supplementary Table 1: Linear fitting parameters of j vs. ν in the non-Faradaic region for ECSA estimation. Experiments were repeated for three samples of each electrode type, and the reported parameters represent the average (avg) and standard deviation (std) of the results.

Metric	**NF_{o_avg}**	**NF_{o_std}**	**NF_{acid_avg}**	**NF_{acid_std}**	**NF_{Fe_avg}**	**NF_{Fe_std}**
Anodic C_{dl}, µF cm^{-2}	31.22	1.53	9.71	0.47	20.00	0.41
Cathodic C_{dl}, µF cm^{-2}	-31.63	1.48	-9.65	0.40	19.64	0.38
Anodic R^2	0.9955	-	0.8845	-	0.9965	-
Cathodic R^2	0.9967	-	0.8923	-	0.9966	-

Supplementary Table 2: Allometric fitting parameters of j vs. ν in the non-Faradaic region for ECSA estimation. Experiments were repeated for three samples of each electrode type, and the reported parameters represent the average (avg) and standard deviation (std) of the results.

Metric	**NF_{o_avg}**	**NF_{o_std}**	**NF_{acid_avg}**	**NF_{acid_std}**	**NF_{Fe_avg}**	**NF_{Fe_std}**
Anodic C_{dl}, µF cm^{-2}	45.88	5.05	72.36	0.47	93.90	0.43
Cathodic C_{dl}, µF cm^{-2}	-49.52	0.85	-68.66	0.40	-80.58	0.38
Anodic α	0.94	-	0.69	-	0.78	-
Cathodic α	0.93	-	0.69	-	0.81	-
Anodic R^2	0.9965	-	0.9969	-	0.9997	-
Cathodic R^2	0.9999	-	0.9994	-	0.9972	-

Supplementary Table 3: Fitting parameters for Ni $2p_{3/2}$, Fe $2p_{3/2}$, and O 1s signals.[8,10,11]

Ni $2p_{3/2}$	Ni	Ni	Ni	NiO	NiO	NiO	NiO
Position (eV)	852.5-852.6	856.2-856.3	858.6-858.7	853.8-854.0	855.5-855.7	861.0-861.2	864.0-864.1
FWHM (eV)	1.3-1.5	2.6-2.9	2.6-2.9	1.3-1.5	2.6-3.0	3.8-4.0	3.0-3.8
% Gauss	0	90	90	90	90	90	90

Ni $2p_{3/2}$	NiOOH	NiOOH	NiOOH	NiOOH	NiOOH	NiOOH
Position (eV)	855.1-855.2	855.8-855.9	856.2-856.3	857.0-857.1	858.3-858.4	861.6-861.7
FWHM (eV)	1.2-1.4	1.3-1.5	1.3-1.5	1.6-1.8	1.6-1.8	4.0-4.4
% Gauss	90	90	90	90	90	90

Fe $2p_{3/2}$	Fe	FeO	FeO	FeO	FeO	FeO
Position (eV)	706.7-706.9	708.2-708.3	709.5-709.6	710.7-710.8	712.1-712.2	715.2-715.3
FWHM (eV)	1.4-1.5	1.2-1.4	1.3-1.5	1.4-1.6	2.0-2.2	1.0-1.5
% Gauss	90	90	90	90	90	90

Fe $2p_{3/2}$	FeOOH	FeOOH	FeOOH	FeOOH	FeOOH	FeOOH
Position (eV)	710.2-710.3	711.4-711.5	712.5-712.6	714.0-714.1	715.5-715.6	719.2-719.3
FWHM (eV)	1.7-1.9	1.8-2.0	1.8-2.0	1.8-2.0	2.0-2.2	3.5-4.0
% Gauss	90	90	90	90	90	90

O 1s	O^{2-}	OH^-	$H_2O_{(ads)}$	C–O*
Position (eV)	529.7-529.8	531.3-531.4	534.7-534.8	533.2-533.3
FWHM (eV)	1.8-2.0	2.0-2.2	1.8-2.00	2.0-2.2
% Gauss	30	30	30	30

References

1 R. A. Marquez, E. Kalokowski, M. Espinosa, J. T. Bender, Y. J. Son, K. Kawashima, C. E. Chukwuneke, L. A. Smith, H. Celio, A. Dolocan, X. Zhan, N. Miller, D. J. Milliron, J. Resasco and C. B. Mullins, *Energy Environ Sci*, 2024, **17**, 2028–2045.

2 M. Frederiksen, R. Chalil Oglou, J. V. Lauritsen, A. Bentien and L. P. Nielsen, *Electrochim Acta*, 2024, **482**, 143988.

3 Y. Yoon, B. Yan and Y. Surendranath, *J Am Chem Soc*, 2018, **140**, 2397–2400.

4 D. M. Morales and M. Risch, *Journal of Physics: Energy*, 2021, **3**, 034013.

5 Z. Sun and J. V. Lauritsen, *Review of Scientific Instruments*, 2021, **92**, 094101.

6 J. Balajka, J. Pavelec, M. Komora, M. Schmid and U. Diebold, *Review of Scientific Instruments*, 2018, **89**, 083906.

7 J. Balajka, M. A. Hines, W. J. I. DeBenedetti, M. Komora, J. Pavelec, M. Schmid and U. Diebold, *Science*, 2018, **361**, 786–789.

8 M. C. Biesinger, B. P. Payne, A. P. Grosvenor, L. W. M. Lau, A. R. Gerson, R. St and C. Smart, *Appl Surf Sci*, 2011, **257**, 2717–2730.

9 R. Chalil Oglou, M. Ceccato, M. L. Frederiksen, A. Shavorskiy, A. Bentien and J. V. Lauritsen, *ACS Catal*, 2025, **15**, 17122–17132.

10 F. Longo, E. Billeter, S. Kazaz, A. Cesarini and M. Nikolic, *Surf Sci*, 2024, **739**, 122397.

11 M. C. Biesinger, B. P. Payne, L. W. M. Lau, R. St and C. Smart, *Surface and Interface Analysis*, 2009, **41**, 324–332.